



HHS Public Access

Author manuscript

Nat Biomed Eng. Author manuscript; available in PMC 2017 September 27.

Published in final edited form as:

Nat Biomed Eng. 2016 ; 1: . doi:10.1038/s41551-016-0006.

A Transistor-like pH Nanoprobe for Tumour Detection and Image-guided Surgery

Tian Zhao¹, Gang Huang¹, Yang Li¹, Shunchun Yang¹, Saleh Ramezani², Zhiqiang Lin¹, Yiguang Wang¹, Xinpeng Ma¹, Zhiqun Zeng¹, Min Luo¹, Esther de Boer³, Xian-Jin Xie⁴, Joel Thibodeaux⁵, Rolf A. Brekken⁶, Xiankai Sun², Baran D. Sumer^{7,*}, and Jinming Gao^{1,*}

¹Department of Pharmacology, Simmons Comprehensive Cancer Center, University of Texas Southwestern Medical Center, 5323 Harry Hines Blvd., Dallas, Texas 75390, USA ²Department of Radiology, University of Texas Southwestern Medical Center, 5323 Harry Hines Blvd., Dallas, Texas 75390, USA ³University Medical Center Groningen, Department of Surgery, Hanzeplein 1, 9713 GZ Groningen, Netherlands ⁴Department of Clinical Science, University of Texas Southwestern Medical Center, 5323 Harry Hines Blvd., Dallas, Texas 75390, USA ⁵Department of Pathology, University of Texas Southwestern Medical Center, 5323 Harry Hines Blvd., Dallas, Texas 75390, USA ⁶Department of Surgery, University of Texas Southwestern Medical Center, 5323 Harry Hines Blvd., Dallas, Texas 75390, USA ⁷Department of Otolaryngology, University of Texas Southwestern Medical Center, 5323 Harry Hines Blvd., Dallas, Texas 75390, USA

Abstract

Because of profound genetic and histological differences in cancerous tissue, it is challenging to detect a broad range of malignant tumours at high resolution. Here, we report the design and performance of a fluorescent nanoprobe with transistor-like responses (transition pH = 6.9) for the detection of the deregulated pH that drives many of the invasive properties of cancer. The nanoprobe amplifies fluorescence signal in the tumour over that in the surrounding normal tissues, resulting in a discretized, binary output signal with spatial resolution smaller than 1 mm. The

Users may view, print, copy, and download text and data-mine the content in such documents, for the purposes of academic research, subject always to the full Conditions of use: http://www.nature.com/authors/editorial_policies/license.html#terms

Correspondence and requests for materials should be addressed to B.D.S. (baran.sumer@utsouthwestern.edu) or J.G. (jinming.gao@utsouthwestern.edu).

Data availability

The authors declare that all the data supporting the findings of this study are available within the paper and its supplementary information.

Supplementary Information is available in the online version of the paper.

Author Contributions

T.Z., B.D.S. and J.G. are responsible for all phases of the research. G.H., S.Y., M.L. and Z.Z. assisted animal surgery, tumour margin analysis and safety evaluation. Y.L. helped develop the transistor concept and performed TEM analysis. S.R. and X.K.S. designed the FDG-PET experiment and performed image analysis. Z.Q.L. performed the imaging comparison of PINS with other commercial probes. Y.G.W. and E.B. helped with fluorescence imaging and X.P.M. assisted with the design and synthesis of the PEPA polymer. B.D.S. and T.Z. performed the survival surgery in mice bearing head and neck cancer and breast cancer, respectively. X.J.X. performed the statistical analysis. J.T. interpreted the histology slides. R.A.B. helped establish genetic pancreatic models and histology interpretations.

Competing Financial Interests

B.D.S. and J.G. are scientific co-founders of OncoNano Medicine, Inc.. The authors declare competing financial interests: details accompany the full-text HTML version of the paper at <http://www.nature.com/natbiomedeng/>

nanoprobe allowed us to image a broad range of tumours in mouse models using a variety of clinical cameras, and to perform real-time tumour-acidosis-guided detection and surgery of occult nodules ($< 1 \text{ mm}^3$) in mice bearing head-and-neck or breast tumours, significantly lengthening mice survivability. We also show that the pH nanoprobe can be used as a reporter in a fast, quantitative assay to screen for tumour-acidosis inhibitors. The binary delineation of pH achieved by the nanoprobe promises to improve the accuracy of cancer detection, surveillance and therapy.

Cancer is a heterogeneous disease that displays diverse inter- as well as intra-tumoural genetic and phenotypic variations from non-transformed cells.¹ Molecular imaging of cancer-specific biomarkers offers the exciting opportunity for tumour detection at the earliest onset of disease and has rapidly advanced the preclinical and clinical development of a variety of imaging probes. Most common strategies have focused on cell-surface receptors such as folate receptor- α (FR- α),² chlorotoxin,³ epidermal growth factor receptor (EGFR),⁴ human epidermal growth factor receptor 2 (Her2/neu),⁵ and tumour associated antigens (e.g. prostate-specific membrane antigen, PSMA).⁶ Although molecular diagnosis of these differences is useful to stratify patients towards personalized therapy, their ability to diagnose a wide range of cancers is often not possible because of genetic or phenotypic heterogeneity (for example, $<25\%$ of breast cancer patients have Her2/neu expression).^{7, 8} In contrast to the diverse genotypes/phenotypes, deregulated energetics is a hallmark of cancer and represents a common pathway that is found in many types of cancer.⁹ The best characterized alteration of energy metabolism in cancer cells is aerobic glycolysis (aka the Warburg effect), where cancer cells preferentially take up glucose and convert it into lactic acid.¹⁰ The clinical significance of the Warburg effect has been shown by the wide use of 2-deoxy-2-[¹⁸F]fluorodeoxyglucose (FDG) in positron emission tomography (PET, >1.5 million annual procedures in the United States alone), which leverages the high glucose uptake of cancer cells.¹¹

Dysregulated pH is emerging as another ubiquitous characteristics of cancer as a result of deregulated tumour metabolism.¹² Cancer cells display a reversed pH gradient with a constitutively increased cytosolic pH and decreased extracellular pH (pH_e) compared to normal tissues regardless of their tissue origin and genetic background. The decreased pH_e ,^{13, 14} or tumour acidosis in the microenvironment, promotes extracellular matrix remodeling and stimulates acid-activated proteases for increased cancer local invasion and metastasis. Previously, we have reported the development of a cyclo(Arg-Gly-Asp-D-Phe-Lys) (cRGDfK)-encoded, Cy5.5-conjugated pH-activatable nanoprobe to image solid tumours.¹⁵ In this study, we simplified the previous nanoprobe design by removing the cRGDfK ligand and replacing the Cy5.5 dye with indocyanine green (ICG), a fluorophore approved for clinical use by the Food and Drug Administration (FDA) in the United States. The resulting pH-activatable indocyanine green-encoded nanosensor (PINS) improved the sharpness of pH response (e.g., $\text{pH}_{10-90\%}$ decreased from 0.26 to 0.15) while allowing deeper fluorescence penetration in tissues due to the longer wavelength of the ICG. PINS serves as a self-contained polymeric nanoprobe that acts as a “chemical transistor” with sharp on and off response that is analogous to the gating of electronic transistors (Fig. 1a). PINS was able to detect a variety of tumours using existing clinical cameras. Real-time, image-guided resection of established tumours as well as occult nodules ($<1 \text{ mm}^3$) in mouse

models resulted in significantly improved long-term survival after cancer surgery. The ability of pH transistor nanoprobe to transform pH from an analog biologic signal to discrete exponentially amplified output radically alters the current imaging paradigm for cancer diagnosis, surveillance and therapy.

Design and synthesis of PINS

We synthesized the PINS nanoprobe consisting of poly(ethylene glycol)-*b*-poly(ethylpropylaminoethyl methacrylate) copolymers (PEG-*b*-(PEPA_x-*r*-ICG_y), *x* and *y* indicate the number of repeating units of EPA monomer and ICG dye, respectively; Supplementary Fig. 1). We systematically investigated the effect of polymer chain length and ICG density on the transition pH, sharpness of response, fluorescence activation ratio and diameter of the nanoprobe (Supplementary Tables 1–2). Increasing the repeating units of PEPA from 40 to 120 resulted in sharper pH transitions (e.g., $pH_{ON/OFF}$ decreased from 0.30 to 0.13, respectively) and slightly lower pH transitions (from 6.96 to 6.91, respectively). The particle diameter increased (20 to 30 nm) with the increase of PEPA length. ICG dye ($\lambda_{ex}/\lambda_{em}=780/820$ nm) was conjugated to the PEPA segment at different densities (0.5, 1 and 2 average ICGs per polymer chain). Higher ICG conjugation number resulted in sharper pH transitions and higher fluorescence activation ratios. Meanwhile, 2 ICGs per polymer chain also reduced the fluorescence intensity at pH 6.5 (on state) due to the increased formation of H-dimers as indicated by larger shoulder peak at 750 nm (Supplementary Figure 1i). Based on these results, we chose PEG-*b*-P(EPA₁₀₀-*r*-ICG₁) as the optimal PINS composition (hydrodynamic diameter 26.0±1.1 nm) for subsequent animal studies. A 3D plot of fluorescence intensity as a function of pH and nanoprobe concentration illustrates the orthogonal pH-modulated fluorescence activation where ICG signal is abolished at blood pH (7.4) but dramatically activated at lower pH (Supplementary Fig. 2a). Above pH 6.9, hydrophobic micellization and homo fluorescence resonance energy transfer (homoFRET)-induced quenching¹⁶ result in annihilation of fluorescence. Below pH 6.9, PINS is dramatically activated due to micelle dissociation into individual unimers as supported by transmission electron microscopy (TEM) analysis (Supplementary Fig. 2c). The divergent protonated unimer and neutral micelle states¹⁷ resemble the phase separation behaviors as in the P- and N-type semiconductors in the electronic transistors (Supplementary Fig. 3).¹⁸ This binary (off/on) pH threshold sensor design is crucial to amplify the persistent but variable acidic tumour pH_c (6.5–6.9, avg. 6.84)¹⁴ with signal suppression in blood (pH 7.4).

PINS achieves broad tumour detection accuracy

Initial dose-response study using a clinical SPY Elite[®] camera established 2.5 mg/kg as the optimal dose of PINS with large tumour/muscle contrast (CNR=27) and a persistent time window (12–24 h) for detection in mice bearing human head/neck HN5 orthotopic tumours (Supplementary Fig. 4, Table 3). Besides HN5 tumours, we imaged additional orthotopic head/neck tumours (FaDu and HCC4034, the latter from a patient of B.D.S), a subcutaneous breast tumour (MDA-MB-231), an intramammary orthotopic breast tumour (triple negative 4T1), a peritoneal metastasis model from HCT116 colorectal cancer, a patient derived xenograft (PDX) of kidney cancer, an orthotopic brain tumour from U87 glioma and two transgenic pancreatic ductal adenocarcinoma models (KIC and KPC). All non-transgenic

tumours were established in non-obese diabetic-severe combined immunodeficiency (NOD-SCID) mice except 4T1 tumours in BalB/C mice. We observed bright tumour illumination across all the tumour types (Fig. 1b and Supplementary Fig. 5). *Ex vivo* imaging revealed high contrast ratios of tumour over muscle (20–50 fold, Supplementary Fig. 6). Using HN5 tumour model, we also demonstrated the compatibility of PINS with multiple clinical cameras (Supplementary Fig. 7). Comparison of PINS with other commercially available near infrared (NIR) probes (800CW-conjugated 2-deoxy-D-glucose (2-DG), cRGD, EGF) at equivalent dye dose showed superior imaging efficacy with PINS (Fig. 2). ICG-loaded PEG-*b*-poly(lactic acid) (PEG-PLA) micelles and free ICG didn't show observable tumour contrast.

To investigate whether PINS can enhance the outcome of FDG-PET, we performed FDG-PET imaging in head and neck tumour bearing mice followed by PINS imaging. In FDG-PET, brain, brown adipose tissues and other hypermetabolic tissues are known to avidly take up glucose resulting in false positives, a common problem with clinical PET (Supplementary Fig. 8).^{19, 20} For tumour detection, although FDG-PET detected large HN5 tumours (~200 mm³), it was not successful at detecting small tumour nodules (~10 mm³, Supplementary Fig. 8b and Supplementary Tables 4). In contrast, all tumour sizes were clearly visible by PINS with high tumour to muscle contrast (CNR>20). *Ex vivo* signals for brain, brown adipose tissues, kidney or other FDG-PET-positive tissues were low (Supplementary Fig. 6). Furthermore, PINS was able to delineate tumour margins at submillimeter spatial resolutions (Fig. 3). These data suggest that PINS can be used as an adjuvant tool to improve the accuracy of tumour staging following FDG-PET. Due to the limitation of light penetration in tissues, PINS will be particularly useful in the imaging of superficial tumours such as skin cancer or peritoneal metastasis (through a laparoscope).

We investigated the colocalization of PINS signals with tumour boundaries at the microscopic level (Supplementary Fig. 9a). HN5 tumour with green fluorescent protein (GFP)-labelled cancer cells and surrounding muscle tissues were collected for frozen sections (8 µm in thickness) 24 h after intravenous PINS injection. ICG fluorescence from PINS illustrates excellent overlap with GFP signals from HN5 cancer cells, which was further validated by H&E histology. To evaluate the contribution of dose accumulation on tumour contrast, we synthesized ³H-labelled PINS through acetylation (-COCT₃) of the free amino groups in the copolymer.¹⁵ At 24 h after ³H-labelled PINS injection, tumour and normal muscle tissues were collected. Nanoprobe accumulation in tumour over normal tissues was highly variable between animals (2 to 10-fold) as measured by ³H radioactivity. In contrast, PINS fluorescence signals were able to discretize tumour vs. normal tissues due to signal amplification through pH activation (Supplementary Fig. 9b). Cellular imaging of activated PINS in HN5 tumour frozen sections further showed punctate signals inside cancer cells (Supplementary Fig. 9c), which indicate nanoprobe internalization inside acidic subcellular organelles (e.g., lysosomes) for sustained tumour contrast.

Tumour acidosis guided surgery by PINS improves survival

We performed real-time tumour acidosis guided surgery (TAGS) using the SPY camera in mice bearing HN5 head and neck or 4T1 breast cancers (Movies 1–2). PINS (2.5 mg/kg)

was injected intravenously 12–24 h before surgery. In a representative operation in HN5 tumour-bearing mice, after resection of the primary tumour, the residual tumour was clearly visible by the SPY camera (Movie 1, also middle left panel in Fig. 4a) but not under white light (top left panel). To validate the accuracy of margin delineation in a surgical setting, we performed non-survival surgery in 9 mice bearing HN5 head and neck tumours using a double blind protocol. The surgeon (B.D.S.) resected the tumours under PINS illumination and marked the tissue specimen (2–3 mm in size) as either primary tumour (fluorescence positive), tumour margin, or tumour-negative muscle tissue (fluorescence negative) in the tumour bed. Frozen sections were made from all specimens, followed by hematoxylin and eosin (H&E) staining. Histological evaluation was performed independently by a surgical pathologist (J.T.) (Supplementary Fig. 10). PINS assessment accuracy was validated on all of the 27 tissue specimens by histologic interpretation. This observed 100% confirmation rate (100% sensitivity and 100% specificity, Supplementary Table 5) represents a 95% confidence with a lower bound of 89.5%. Long-term survival surgery outcomes show improved loco-regional control and overall survival with TAGS over white light surgery (WLS), debulking surgery and untreated controls (Fig. 4b). Debulking surgery with macroscopically positive margins typically provides no survival benefit for head and neck cancer and served as a control for the adequacy of WLS. WLS was superior to the debulking and untreated controls ($P < 0.0001$), indicating good unbiased technique. TAGS led to the best outcome, with 13 out of 18 animals (72%) showing cures 150 days post-operatively ($P < 0.0001$ vs. WLS, Fig. 4b, Supplementary Table 6).

To mimic clinical scenarios where identifying occult cancerous nodules is critical, we established small orthotopic breast tumours in immunocompetent female BalB/C mice. We injected 5×10^4 triple negative 4T1 breast cancer cells in the inguinal mammary pad. With an estimated doubling time of 24 h, the nodule size represents < 1 million 4T1 cells in the foci on day 4. PINS under SPY camera was able to identify the subcutaneous 4T1 foci through the skin, which was confirmed by histology (Fig. 5a–c). Tumour could not be detected with visual inspection or palpation. For the white light control, we allowed the tumour to grow to $\sim 25 \text{ mm}^3$ to be visible, and carefully resected the primary tumour and surrounding margin. TAGS (Movie 3) resulted in superior visualization, improving survival after resection over the untreated control and WLS ($P < 0.05$, Fig. 5d, Supplementary Table 6), demonstrating superb imaging sensitivity with PINS.

PINS facilitates screening of acidosis inhibitors

Tumour response to small molecular inhibitors targeting different tumour acidosis pathways was evaluated by PINS (Fig. 6). We selected four inhibitors: acetazolamide for carbonic anhydrase IX (CAIX),²¹ α -cyano-4-hydroxycinnamate (CHC) for monocarboxylate transporter (MCT),²² cariporide for sodium proton exchanger 1 (NHE1)²³ and pantoprazole as a proton pump inhibitor (PPI)²⁴. PINS was injected intravenously to SCID mice bearing HN5, 4T1 or A549 tumours following inhibitor administration. NIR imaging 24 h after PINS injection showed greatest inhibition (50–80%) by CAIX inhibitor acetazolamide over phosphate-buffered saline (PBS) control in all three models. Other inhibitors showed less pronounced and more variable inhibitions in these tumour models. The PINS response is consistent with previously reported antitumour efficacy of CAIX inhibitors in tumour

bearing mice.^{25, 26} Compared to $^1\text{H}/^{31}\text{P}^{27}$ or hyperpolarization ^{13}C magnetic resonance imaging (MRI) methods²⁸, PINS imaging offers a simple and quantitative assay for the rapid screening of small molecular drugs targeting tumour acidosis pathways.^{21, 29}

Pharmacokinetic and safety evaluations

To determine the pharmacokinetic and biodistribution profiles of PINS, we injected ^3H -labelled PINS at the same dose (2.5 mg/kg) as the imaging dose. The plasma concentration–time curve showed a two-phase behavior over 24 h (Supplementary Fig. 12a). The α -phase half-lives ($t_{1/2,\alpha}$) was 2.0 ± 1.6 h. The β -phase half-life ($t_{1/2,\beta}$) was 8.6 ± 2.7 h ($n=4$). Biodistribution studies show that tumour accumulation was 2.7 ± 1.9 % of injected dose per gram (ID/g) of tissue. Liver and spleen were the main organs for PINS uptake.

Safety evaluation of PINS in immunocompetent C57BL/6 mice showed temporary body weight loss and acute toxicity response at high dose (Supplementary Fig. 13a and Supplementary Table 7). The maximum tolerated dose was determined to be 250 mg/kg, 100-fold higher than the optimal imaging dose. Mice were sacrificed on day 1, 7 and 28 at 200 and 250 mg/kg. Liver and kidney functions were analyzed (Supplementary Fig. 13b–e). Liver enzyme levels alanine transaminase (ALT) and aspartate aminotransferase (GOT) increased on day 1 after PINS injection and returned to normal after 7 days. Histologic analysis (Supplementary Fig. 14) showed microsteatosis in the liver in the 250 mg/kg group at day 1 and returned to normal by day 28. Other major organs (e.g., kidney, heart, spleen) were normal.

Discussion

Most cancer molecular imaging agents (e.g., mAb-dye conjugates) rely on their bindings to intended cancer targets to increase dose accumulation for observed tumour contrast. Such strategies translate the target concentration into a linearly proportional imaging signal. This analog signal is subject to signal degradation and decreased signal to noise ratio (SNR) when amplified by increasing the dose or detector sensitivity, and can show great inter-test variability because cancer target expressions are highly variable (e.g., EGFR varies widely in head and neck tumours from 0.3 to 97-fold³⁰) with spatial and temporal fluctuations. To overcome these limitations, we have previously reported a signal amplification strategy that is orthogonal to dose accumulation through pH activation in response to angiogenic tumour vasculature and acidic extracellular pH.¹⁵ In this study, we further clarified a pH transistor concept with binary off/on response at a threshold pH (i.e., 6.9) analogous to the electronic transistors with a threshold voltage gating (Supplementary Fig. 3). This transistor concept simplified the understanding of PINS function to switch and amplify variable biological signals into discretized, binary output (Supplementary Fig. 9a). The significance of this conceptual realization became apparent when we performed numerous animal surgeries and were able to appreciate the consistency and robustness of the tumour signal. This level of consistency is rare in biology and was further confirmed when the current PINS had a simplified design without the need to introduce any targeting ligands (e.g., cRGD as in the previous study) to achieve broad tumour imaging efficacy.

Our initial design of PINS with a threshold pH transition at 6.9 was to maximally discretize the analog acidic extracellular pH_e in tumours (6.5–6.9, avg. 6.84)¹⁴ and normal tissue pH (7.4). Studies by ³H-labelled PINS and fluorescence microscopy suggest additional factors also contribute to the tumour contrast. For example, increased dose accumulation of PINS in HN5 tumours was found over muscle tissues (Supplementary Fig. 9b), which may be due to the enhanced permeability and retention (EPR) effect in solid tumours.³¹ It is worth noting pH activation was able to further amplify the variable dose accumulation signal into discrete fluorescence signal between tumour and muscle tissues. In addition, fluorescence microscopy of tumour sections showed activated PINS in subcellular organelles, which may result from increased rates of macropinocytosis of cancer cells as a strategy to catabolize proteins for tumour growth and survival.³² Internalization of PINS (either activated or intact) in acidic organelles such as lysosomes would keep the signal in the on state and also within the tumour cells rather than blurring the surrounding tissue through diffusion. This may explain the sustained imaging contrast over 24 h (Supplementary Fig. 4) as well as the sharp delineation of tumour boundary over the surrounding muscle tissue (Supplementary Fig. 9a). While specific contribution from each input is unclear and may depend on oncogenotypes of tumours, the transistor-like behavior of PINS is able to combine the above contributions into an emergent and persistent tumour vs. normal tissue signal. This ability of PINS to use pH as a trigger to switch and amplify tumour signals is unique from conventional pH sensors (e.g., cell-impermeable 2-imidazole-1-yl-3-ethoxycarbonyl propanic acid (IEPA) and 3-aminopropylphosphonate (3-APP))²⁷ designed to measure extracellular pH of solid tumours. Compared to these small molecular pH tracers, although PINS loses fine gradations of information (e.g., ability to differentiate 6.5 vs. 6.8), its tradeoff is in the maximization of detection sensitivity by turning on and integrating all the pH signals below 6.9. This signal dichotomization strategy proves essential in achieving real-time image-guided surgery of solid tumours (Movies 1–3) as well as detection of small occult diseases (Fig. 5).

Surgical resection is a cornerstone of therapy for patients with solid cancers. For head and neck cancer, the complex mechanisms involved with speech and swallowing, the prevention of aspiration, and maintenance of the airway place a premium on surgical margins.³³ Breast conserving lumpectomies are increasingly performed in 60–70% of patients. Repeat surgery rates due to inadequate tumour removal though are quite high (20–25%) especially in patients with larger tumours, positive axillary nodes, tumours with a lobular histology or with an extensive intraductal component.^{34–37} A variety of exogenous fluorophores have been developed for intra-operative margin assessment. Many of these agents are restricted to specific receptor expression profiles thereby lack broad detection capability. Receptor-targeted imaging strategies are effective at stratifying patients toward therapy, but do not allow for broad detection of tumours due to the large inter- and intra-tumour heterogeneity of solid tumours. By targeting a ubiquitous signal cancer hallmark in dysregulated pH, PINS has shown broad tumour specificity in a variety of cancer types (head/neck, breast, kidney, pancreatic, brain, peritoneal metastasis) and various mouse tumour models (transgenic, patient derived xenograft, and orthotopic xenograft). The high spatio-temporal sensitivity allowed real-time, image-guided surgery of head/neck and breast cancers (Movies 1–3), which significantly improved accuracy in pathological validation of tumour margins (Fig. 4a). Achieving a tumour-free surgical margin with functional preservation of normal tissues

is becoming an important objective during surgery. Based on the high resolution capability of PINS in delineation of tumour margins, we performed TAGS resection with >70% cures in a head and neck tumour models and demonstrated the ability to remove small occult nodules in a triple negative breast cancer model. Accurate tumour margin delineation is a prerequisite for precise image-guided resection of tumour. Although most cancer surgeries do not require submillimeter resolution, real-time, high resolution visualization of tumours can still help decision making in the operating room. This is particularly useful in the visualization of infiltrating lesions that were indeed detected in our experiments (Movie 1), where this additional detection was responsible for at least part of the observed survival differences of TAGS over white light surgery (Fig. 4b).

In summary, results from this study establish pH transistor nanoprobe as a broadly applicable strategy to allow highly sensitive, cancer-specific detection of malignant tumours. The ability of PINS to detect a range of tumours offers a broad image-guided strategy to improve tumour surgery. High resolution, real-time delineation of tumours using clinical cameras have led to improved cancer detection and eradication in selected head/neck and breast cancers. Key to this robust detection is the dichotomization of the output signal in response to a predetermined threshold in the input variable. This chemical digitization process removes ambiguity related to fluctuations or variability in the input biologic signal because of gating, which in turn minimizes noise. Potential challenges that may limit universal applicability of the nanoprobe in the clinics include lack of fluorescence in benign, slow growing, or necrotic tumours and physical limitation of light penetration in biological tissues. Nevertheless, we anticipate this imaging paradigm will deliver broad impact in cancer staging, image-guided biopsy or surgery, and will be used as a reporter assay for monitoring response of drugs targeting tumour acidosis.

Methods

Synthesis and characterization of PINS

EPA monomer was synthesized following the reported procedure³⁸: 2-(ethylpropylamino)ethanol (26.2 g, 0.2 mol) and trimethylamine (27.9 mL, 0.2 mol) were dissolved in 200 mL dichloromethane and then methacryloyl chloride (19.4 mL, 0.2 mol) was added dropwise at 0 °C. The reaction was left overnight at room temperature. The solvent was then removed by rotovap and the resulting residue was distilled *in vacuo* as a colorless liquid. PEG-*b*-(PEPA_x-*r*-ICG_y) copolymer was synthesized using the atom transfer radical polymerization method.³⁹ In a typical procedure, EPA monomer (797.2 mg, 4 mmol), 2-aminoethyl methacrylate hydrochloride (50.0 mg, 0.3 mmol), N,N,N',N'',N''-pentamethyldiethylenetriamine (PMDETA) (8.4 μL, 0.04 mmol), and MeO-PEG₁₁₄-Br (200.0 mg, 0.04 mmol) were charged into a polymerization tube. Then a mixture of 2-propanol (1 mL) and DMF (1 mL) was added to dissolve the monomer and initiator. After three cycles of freeze-pump-thaw to remove oxygen, CuBr (5.8 mg, 0.04 mmol) was added into the reaction tube under nitrogen atmosphere, and the tube was sealed *in vacuo*. The polymerization was carried out at 40 °C for 12 h. After polymerization, the reaction mixture was diluted with 10 mL tetrahydrofuran (THF), and passed through an Al₂O₃ column to remove the catalyst. The THF solvent was removed by rotovap. The residue was dialyzed in

distilled water and lyophilized to obtain a white powder. ICG was conjugated to the primary amino groups on the polymer via N-hydroxysuccinimide (NHS)-ester chemistry.⁴⁰ The PINS nanoprobe was produced by a solvent evaporation method.¹⁵ The final product was either concentrated to a 2.5 mg/mL aqueous stock solution for further usage or lyophilized for storage. Transmission electron microscopy analysis was carried out on a JEOL 1200EX electron microscope. A Shimadzu UV-Vis spectrophotometer (UV-1800 model) was used to determine the dye content in ICG-conjugated polymer.

FDG-PET/computed tomography (CT) imaging

Animal protocol related to this study was reviewed and approved by the Institutional Animal Care and Use Committee and Radiation Safety Committee. Mouse FDG-PET/CT imaging was performed using a Siemens Inveon PET/CT Multi-Modality System (Siemens Medical Solutions, Knoxville, TN). All animals were fasted for 12 h prior to FDG-PET imaging. Each mouse received 5.55 MBq of FDG in 150 μ L saline intravenously via tail vein injection. The mice were placed on a heat pad before and during image acquisition. PET images were acquired 1 h post-injection, for 15 mins, with animals under 2.5% isoflurane. PET images were reconstructed into a single frame using the 3D Ordered Subsets Expectation Maximization (OSEM3D/MAP) algorithm. CT images were acquired immediately after PET. CT projections (360 steps/rotation) were acquired with a power of 80 kVp, current of 500 μ A, exposure time of 145 ms, binning of 4, and effective pixel size of 102 μ m. PET and CT images were co-registered by the manufacturer's software. Regions of interest (ROI) were drawn manually over the tumour guided by the corresponding CT images. The target activity was calculated as %ID/g and standardized uptake value (SUV) (Supplementary Table 1).

Fluorescence and tumour margin evaluation

Tumour as well as surrounding tissues was collected 24 h after probe injection. The collected samples were frozen in optimum cutting temperature (O.C.T.) medium and 8 μ m frozen section slides were prepared. The PINS fluorescence was imaged using a fluorescence flatbed scanner for 800 nm excitation (Odyssey, LI-COR Biosciences). GFP in the cancer cells were imaged with a Deltavision Deconvolution Microscope and images were stitched afterwards. H&E staining were performed after all fluorescent images were collected. The margins of the tumours were determined by a clinical pathologist (J.T.) from H&E staining. PINS fluorescent intensity and surrounding normal tissue fluorescence intensity were measured based on five areas of interest (0.5 mm \times 0.5 mm) for each sample.

Margin validation

Tissue specimens for margin validation were collected using a double blind protocol. Non-survival surgeries were performed with fluorescence guidance under a SPY Elite[®] camera on nine head and neck tumour-bearing mice following a similar procedure for survival surgery except the mice were sacrificed after the surgery. The surgeon resected the tumours under PINS illumination and marked the tissue specimen (2–3 mm in size) as either primary tumour, tumour margin or negative muscle tissue based on fluorescence readings. For each tumour bearing mouse, one tumour specimen, one tumour margin specimen and one negative tumour bed specimen were collected. Frozen sections were prepared from the

specimens for H&E staining and histology validation. Histological evaluation was performed independently by a surgical pathologist without knowing the fluorescence assignment for each sample.

Survival surgery

Survival surgeries were performed in orthotopic HN5 head and neck cancer or 4T1 breast cancer models. All mice were injected with 2.0 mg/kg PINS 12–24 h prior to the surgery. For head and neck cancer surgery, the tumours were allowed to grow to 50 mm³. Before surgery, all mice were randomized by an independent technician: each mouse was randomly picked up from the cage and assigned to control, debulking, WLS or TAGS group in sequence, and the assignment was repeated until all groups reached the designated number of animals. Mice were then anesthetized with 2.5% isoflurane. Hairs were removed with depilatory cream. Mice were prepped and draped in sterile fashion. For the debulking surgery group, the tumours were partially removed. For the WLS group, surgery was performed under white light illumination with the entire ascertainable tumour removed based on the surgeon's best judgement. For the TAGS group, the surgery was performed with fluorescence guidance via a SPY Elite[®] camera. White light illumination was left on for the TAGS group with no interference with ICG imaging. After surgery all animals received analgesic and antibiotics. Body weights were monitored before and after the surgery. Animals were examined for tumour recurrence three times a week. The animal was considered dead if the weight loss was more than 20% of the original body weight or the tumour volume exceeded 1500 mm³. For breast cancer surgery, 5×10⁴ of 4T1 cells were injected into either left or right inguinal mammary pad for tumour inoculation. For the TAGS group the tumours were allowed to grow for 4 days after cancer cell injection. For the WLS the tumours were allowed to grow to a palpable size (25 mm³). All animals were sacrificed on day 150 after surgery without obvious signs of tumour recurrence.

Tumour acidosis inhibition study

SCID mice bearing HN5 tumours of similar sizes were used to evaluate tumour responses to acidosis inhibitors. The mice were injected intravenously with PBS, acetazolamide (40 mg/kg), α -cyano-4-hydroxycinnamate (200 mg/kg), cariporide (25 mg/kg) and pantoprazole (50 mg/kg) 1 h before PINS (2.5 mg/kg) injection. Inhibitors except CHC were administered again 6 h after PINS injection. Mice were imaged with Hamamatsu PDE 24h after probe injection. Tumour fluorescence intensities were measured by Image J and normalized to PBS control.

Statistical analysis

Data were expressed as mean \pm s.d. where $n \geq 5$ and plotted or tabulated as individual data points when $n < 5$. Sample sizes were chosen to ensure adequate power (>85%, at significance of 0.05) to detect predicted effect sizes, which were estimated based on either preliminary data or previous experiences with similar experiments. The confidence interval of PINS detection accuracy was calculated using the exact method (one-sided). Differences between groups were assessed using the unpaired, two-sided Student *t*-test for the calculation of *p*-values. Kaplan-Meier method was used for survival function plot and *p*-values comparing different survival groups were based on Logrank test. Due to the very

small number of multiple comparisons, *p*-values were reported without adjustment. SAS 9.3 for Windows was used for data analysis. **P* < 0.05, ***P* < 0.01, ****P* < 0.001, *****P* < 0.0001.

Supplementary Material

Refer to Web version on PubMed Central for supplementary material.

Acknowledgments

This work is supported by the National Institutes of Health (R01EB013149 and R01CA192221 to J.G.) and Cancer Prevention and Research Institute of Texas (RP140140 to B.D.S. and J.G.). Animal imaging work is supported by the UT Southwestern Small Animal Imaging Resource Grant (U24 CA126608) and Simmons Cancer Center Support Grant (P30 CA142543). We thank J. Sun for animal imaging, L.C. Su for histology analysis, D. Zhao for preparation of U87 brain tumour model, A. Pavia-Jimenez and J. Brugarolas for the renal PDX model, and G. Balch for the peritoneal met model.

References

1. Vogelstein B, et al. Cancer genome landscapes. *Science*. 2013; 339:1546–1558. [PubMed: 23539594]
2. van Dam GM, et al. Intraoperative tumor-specific fluorescence imaging in ovarian cancer by folate receptor- α targeting: first in-human results. *Nat Med*. 2011; 17:1315–1319. [PubMed: 21926976]
3. Veiseh M, et al. Tumor paint: a chlorotoxin: Cy5.5 bioconjugate for intraoperative visualization of cancer foci. *Cancer Res*. 2007; 67:6882–6888. [PubMed: 17638899]
4. Ke S, et al. Near-infrared optical imaging of epidermal growth factor receptor in breast cancer xenografts. *Cancer Res*. 2003; 63:7870–7875. [PubMed: 14633715]
5. Koyama Y, et al. Spectral fluorescence molecular imaging of lung metastases targeting HER2/neu. *Clin Cancer Res*. 2007; 13:2936–2945. [PubMed: 17504994]
6. Nakajima T, et al. Targeted, activatable, in vivo fluorescence imaging of prostate-specific membrane antigen (PSMA) positive tumors using the quenched humanized J591 antibody-indocyanine green (ICG) conjugate. *Bioconjug Chem*. 2011; 22:1700–1705. [PubMed: 21740058]
7. Jacobs TW, Gown AM, Yaziji H, Barnes MJ, Schnitt SJ. HER-2/neu protein expression in breast cancer evaluated by immunohistochemistry. A study of interlaboratory agreement. *Am J Clin Pathol*. 2000; 113:251–258. [PubMed: 10664627]
8. Paik S, et al. HER2 and choice of adjuvant chemotherapy for invasive breast cancer: national surgical adjuvant breast and bowel project protocol B-15. *J Natl Cancer Inst*. 2000; 92:1991–1998. [PubMed: 11121461]
9. Hanahan D, Weinberg RA. Hallmarks of cancer: the next generation. *Cell*. 2011; 144:646–674. [PubMed: 21376230]
10. Heiden MG, Cantley LC, Thompson CB. Understanding the Warburg Effect: The Metabolic Requirements of Cell Proliferation. *Science*. 2009; 324:1029–1033. [PubMed: 19460998]
11. Zhu A, Lee D, Shim H. Metabolic positron emission tomography imaging in cancer detection and therapy response. *Semin Oncol*. 2011; 38:55–69. [PubMed: 21362516]
12. Webb BA, Chimenti M, Jacobson MP, Barber DL. Dysregulated pH: a perfect storm for cancer progression. *Nat Rev Cancer*. 2011; 11:671–677. [PubMed: 21833026]
13. Gillies RJ, Raghunand N, Garcia-Martin ML, Gatenby RA. pH imaging. *IEEE Eng Med Biol Mag*. 2004; 23:57–64.
14. Volk T, Jahde E, Fortmeyer HP, Glusenkamp KH, Rajewsky MF. pH in human tumour xenografts: effect of intravenous administration of glucose. *Br J Cancer*. 1993; 68:492–500. [PubMed: 8353039]
15. Wang Y, et al. A nanoparticle-based strategy for the imaging of a broad range of tumours by nonlinear amplification of microenvironment signals. *Nat Mater*. 2014; 13:204–212. [PubMed: 24317187]

16. Zhou K, et al. Multicolored pH-tunable and activatable fluorescence nanoplatfom responsive to physiologic pH stimuli. *J Am Chem Soc.* 2012; 134:7803–7811. [PubMed: 22524413]
17. Li Y, et al. Molecular basis of cooperativity in pH-triggered supramolecular self-assembly. *Nat Commun.* 2016; 7:13214. [PubMed: 27786266]
18. Bardeen J. Research Leading to Point-Contact Transistor. *Science.* 1957; 126:105–113. [PubMed: 17795477]
19. Cook GJ, Wegner EA, Fogelman I. Pitfalls and artifacts in 18FDG PET and PET/CT oncologic imaging. *Semin Nucl Med.* 2004; 34:122–133. [PubMed: 15031812]
20. Fukui MB, et al. Combined PET-CT in the head and neck: part 2. Diagnostic uses and pitfalls of oncologic imaging. *Radiographics.* 2005; 25:913–930. [PubMed: 16009815]
21. Neri D, Supuran CT. Interfering with pH regulation in tumours as a therapeutic strategy. *Nat Rev Drug Discov.* 2011; 10:767–777. [PubMed: 21921921]
22. Sonveaux P, et al. Targeting lactate-fueled respiration selectively kills hypoxic tumor cells in mice. *J Clin Invest.* 2008; 118:3930–3942. [PubMed: 19033663]
23. Cardone RA, Casavola V, Reshkin SJ. The role of disturbed pH dynamics and the Na⁺/H⁺ exchanger in metastasis. *Nat Rev Cancer.* 2005; 5:786–795. [PubMed: 16175178]
24. Vishvakarma NK, Singh SM. Mechanisms of tumor growth retardation by modulation of pH regulation in the tumor-microenvironment of a murine T cell lymphoma. *Biomed Pharmacother.* 2011; 65:27–39. [PubMed: 20685069]
25. Lou Y, et al. Targeting tumor hypoxia: suppression of breast tumor growth and metastasis by novel carbonic anhydrase IX inhibitors. *Cancer Res.* 2011; 71:3364–3376. [PubMed: 21415165]
26. Pacchiano F, et al. Ureido-substituted benzenesulfonamides potently inhibit carbonic anhydrase IX and show antimetastatic activity in a model of breast cancer metastasis. *J Med Chem.* 2011; 54:1896–1902. [PubMed: 21361354]
27. Gillies RJ, Raghunand N, Karczmar GS, Bhujwala ZM. MRI of the tumor microenvironment. *J Magn Reson Imaging.* 2002; 16:430–450. [PubMed: 12353258]
28. Gallagher FA, et al. Magnetic resonance imaging of pH in vivo using hyperpolarized ¹³C-labelled bicarbonate. *Nature.* 2008; 453:940–943. [PubMed: 18509335]
29. Parks SK, Chiche J, Pouyssegur J. Disrupting proton dynamics and energy metabolism for cancer therapy. *Nat Rev Cancer.* 2013; 13:611–623. [PubMed: 23969692]
30. Ang KK, et al. Impact of epidermal growth factor receptor expression on survival and pattern of relapse in patients with advanced head and neck carcinoma. *Cancer Res.* 2002; 62:7350–7356. [PubMed: 12499279]
31. Maeda H, Wu J, Sawa T, Matsumura Y, Hori K. Tumor vascular permeability and the EPR effect in macromolecular therapeutics: a review. *J Controlled Release.* 2000; 65:271–284.
32. Comisso C, et al. Macropinocytosis of protein is an amino acid supply route in Ras-transformed cells. *Nature.* 2013; 497:633–637. [PubMed: 23665962]
33. More YI, et al. Functional swallowing outcomes following transoral robotic surgery vs primary chemoradiotherapy in patients with advanced-stage oropharynx and supraglottis cancers. *JAMA otolaryngology-head & neck surgery.* 2013; 139:43–48. [PubMed: 23247974]
34. Ansher MS, et al. Local failure and margin status in early-stage breast carcinoma treated with conservation surgery and radiation therapy. *Ann Surg.* 1993; 218:22–28. [PubMed: 8328825]
35. Schmidt-Ullrich R, et al. Tumor margin assessment as a guide to optimal conservation surgery and irradiation in early stage breast carcinoma. *Int J Radiat Oncol Biol Phys.* 1989; 17:733–738. [PubMed: 2777663]
36. Solin LJ, Fowble BL, Schultz DJ, Goodman RL. The significance of the pathology margins of the tumor excision on the outcome of patients treated with definitive irradiation for early stage breast cancer. *Int J Radiat Oncol Biol Phys.* 1991; 21:279–287. [PubMed: 1648041]
37. Holland R, et al. The presence of an extensive intraductal component following a limited excision correlates with prominent residual disease in the remainder of the breast. *J Clin Oncol.* 1990; 8:113–118. [PubMed: 2153190]
38. Zhou K, et al. Tunable, ultrasensitive pH-responsive nanoparticles targeting specific endocytic organelles in living cells. *Angew Chem Int Ed Engl.* 2011; 50:6109–6114. [PubMed: 21495146]

39. Matyjaszewski K, Tsarevsky NV. Nanostructured functional materials prepared by atom transfer radical polymerization. *Nat Chem.* 2009; 1:276–288. [PubMed: 21378870]
40. Ma X, et al. Ultra-pH-sensitive nanoprobe library with broad pH tunability and fluorescence emissions. *J Am Chem Soc.* 2014; 136:11085–11092. [PubMed: 25020134]

Author Manuscript

Author Manuscript

Author Manuscript

Author Manuscript

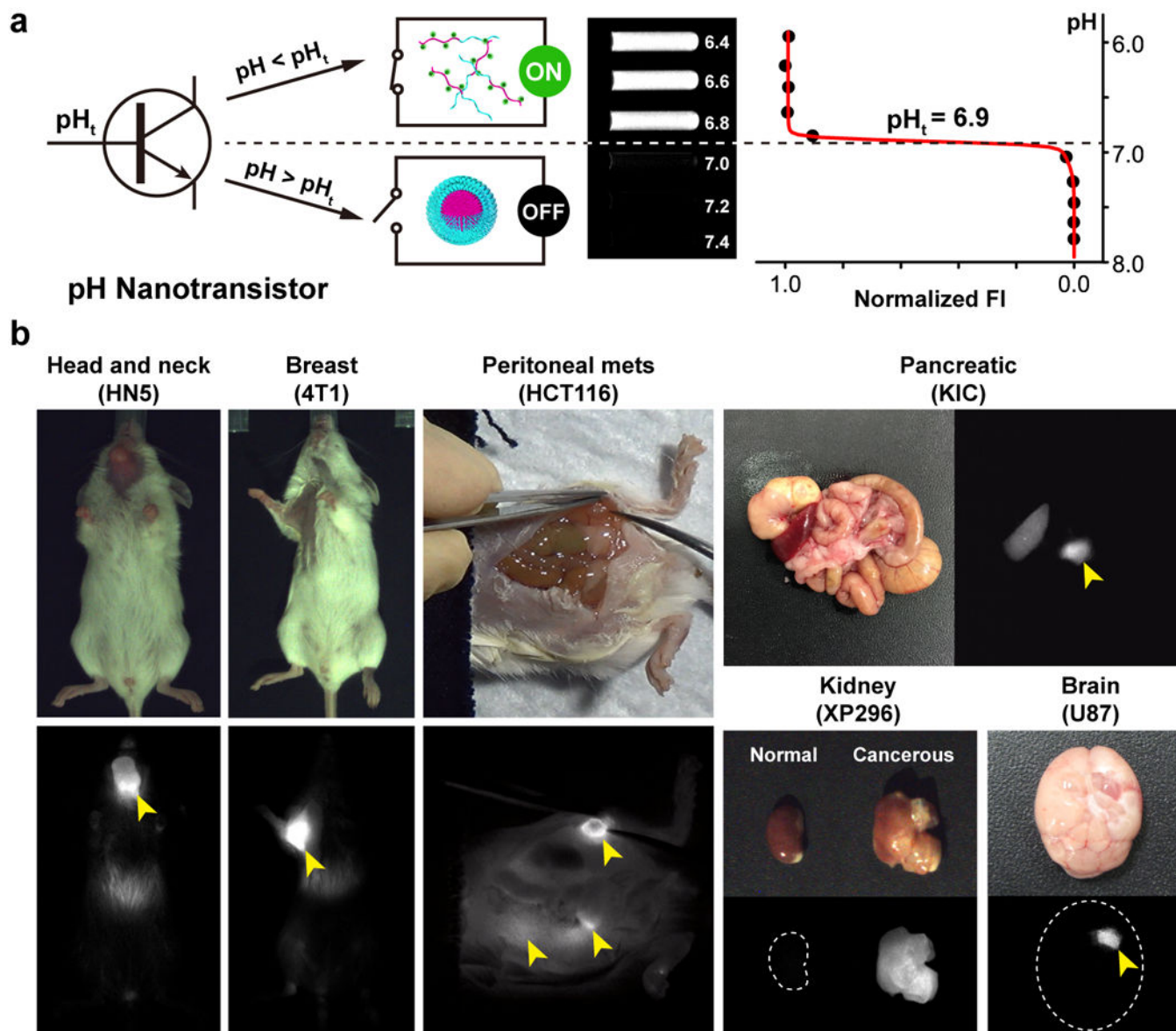


Figure 1. pH transistor nanoprobe achieves broad tumour detection specificity

a, Schematic of pH nanotransistor with binary off/on response at a transition pH of 6.9. At $\text{pH} < 6.9$, nanoprobe dissociates into protonated, highly fluorescent unimers (on state); at $\text{pH} > 6.9$, nanoprobe is silent (off state). **b**, PINS nanoprobe (intravenous injection 24 h prior to imaging by SPY Elite[®] clinical camera) demonstrates broad tumour imaging efficacy in a variety of tumour models (head and neck, breast, peritoneal metastasis, kidney, brain, pancreatic) and organ sites. Yellow arrowheads indicate the location of tumours. Additional tumour models are shown in Supplementary Fig. 5. *Ex vivo* quantification is available in Supplementary Fig. 6.

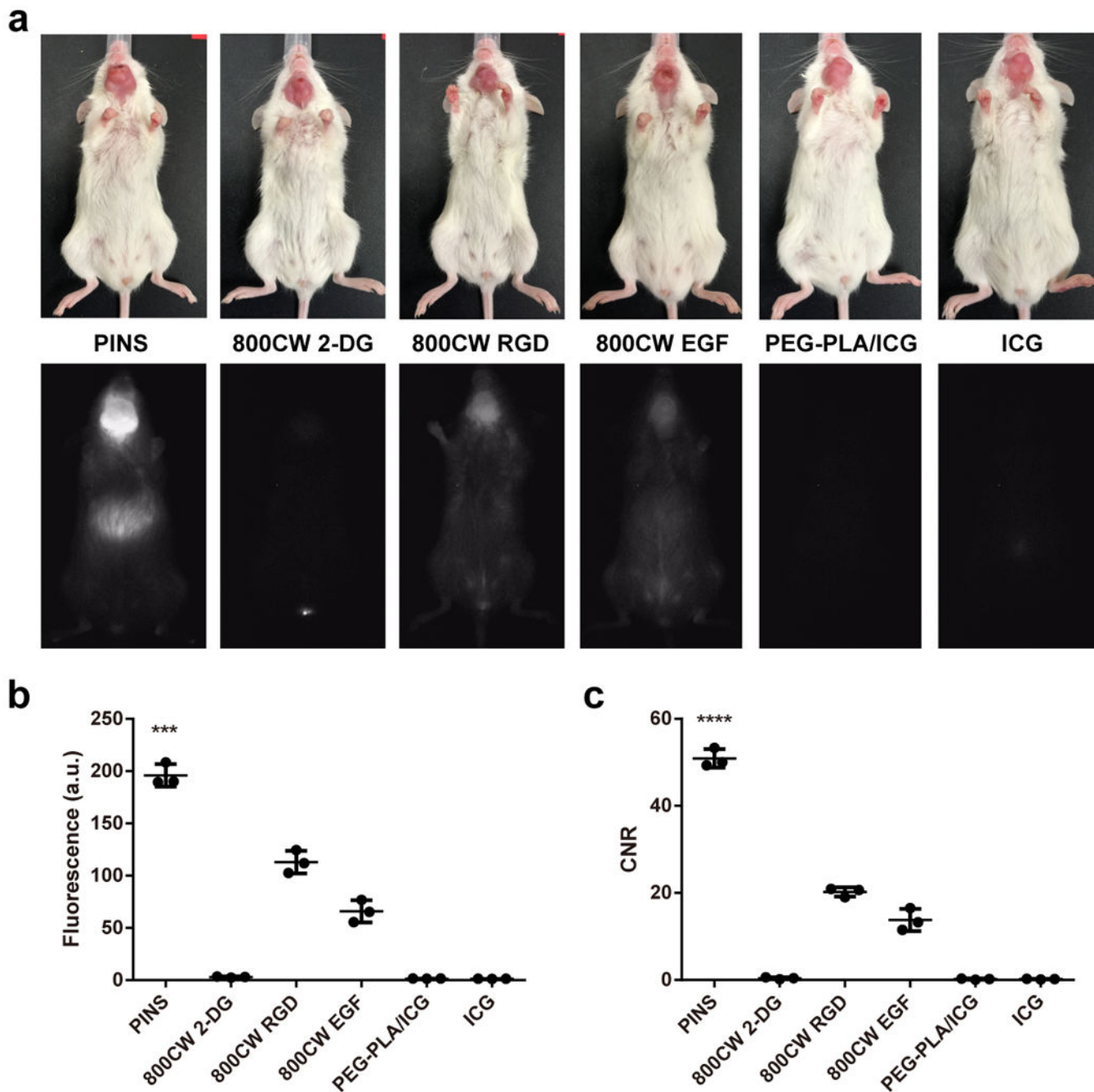


Figure 2. Comparison between PINS and other commercial NIR probes
a, Images of mice bearing HN5 head and neck tumours 24h after different probe injection. The fluorophore doses are the same for all groups. Quantification of the tumour fluorescence intensity (**b**) and contrast to noise ratio (**c**) demonstrate the superior imaging efficacy by PINS over the other imaging probes. Data are presented as mean \pm s.d. ($n = 3$). *** $P < 0.001$, **** $P < 0.0001$, compared with other groups.

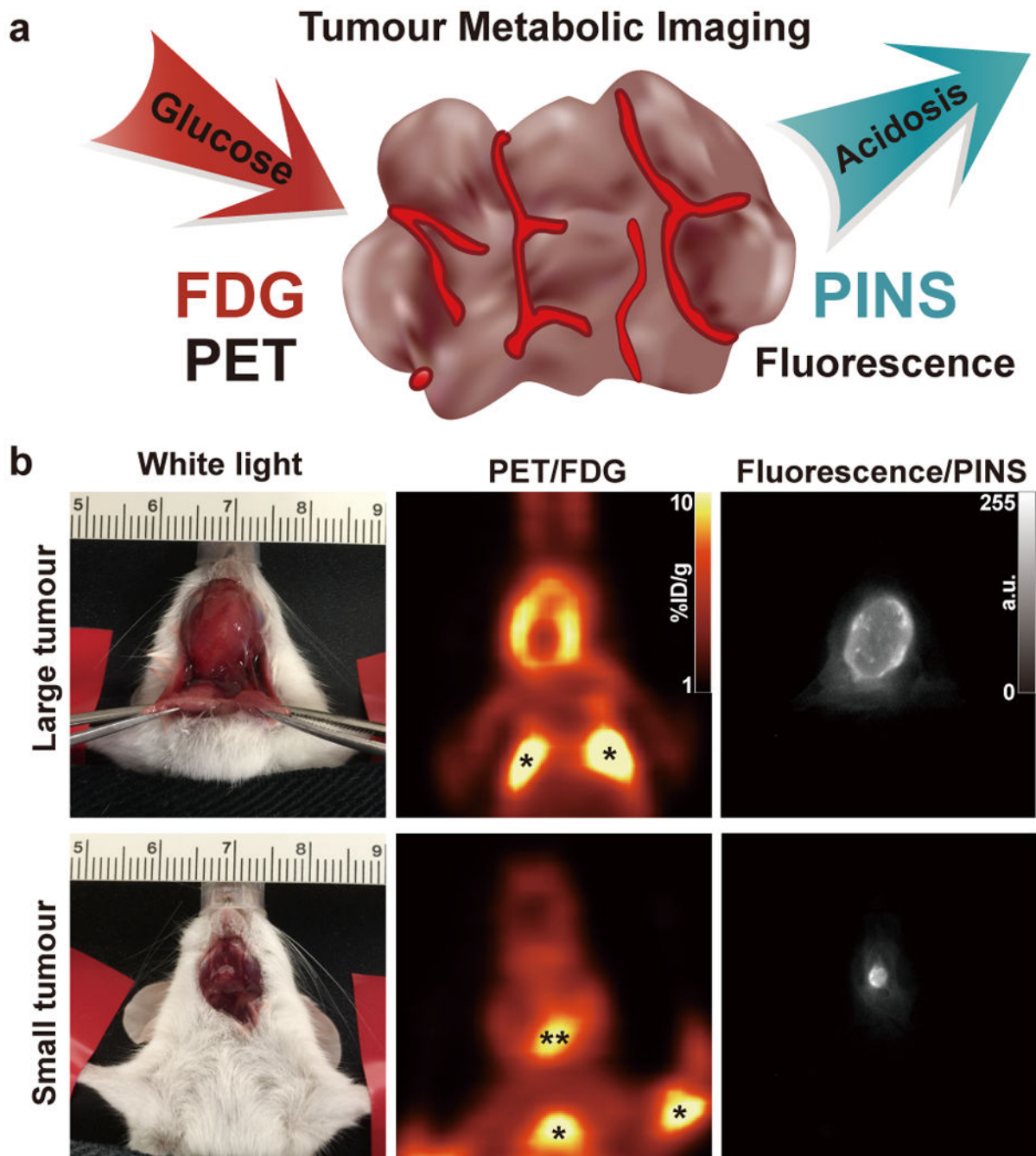


Figure 3. PINS improves cancer detection over FDG-PET

a, Schematic of tumor metabolic imaging by PET with FDG or NIR fluorescence imaging with PINS. **b**, SCID mice bearing large (200 mm^3) or small (10 mm^3) HN5 orthotopic tumours were studied. PINS imaging showed improved sensitivity and specificity of tumour detection over FDG-PET. Asterisks (*) and double asterisk (**) indicate false positive detection of brown fat and striated muscle in the PET images, respectively.

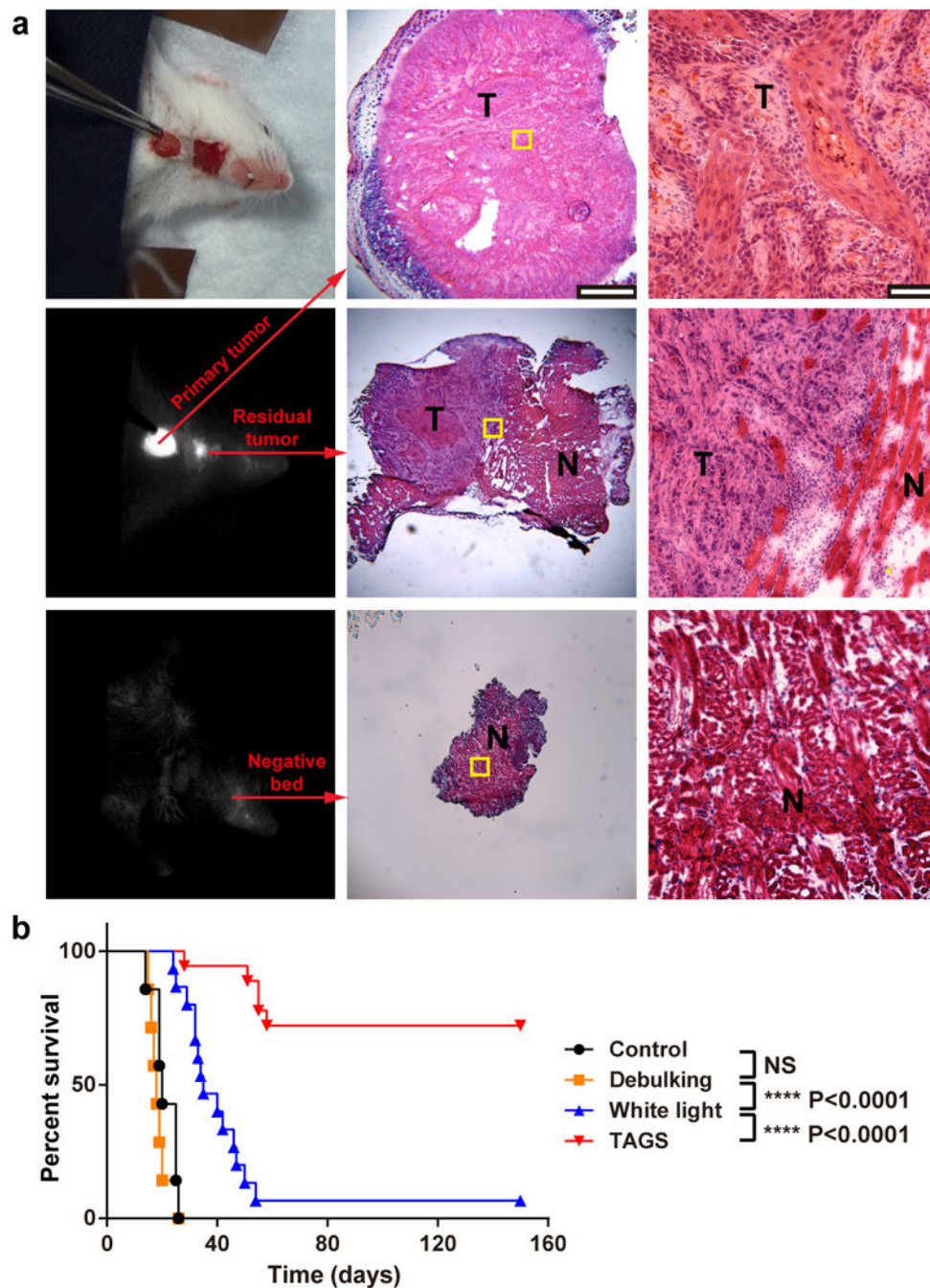


Figure 4. Tumour acidosis guided surgery (TAGS) in mice bearing orthotopic head and neck tumours

a. Surgical resection of primary HN5 tumours and successful detection of residual tumours by SPY Elite[®] camera. Visual inspection of tumour bed by eyes was not able to differentiate residual tumours from surrounding muscle tissue (top left). Tumour tissue (T) and normal tissue (N) were verified by histology. Scale bar = 1 mm (low magnification) or 100 μ m (high magnification). **b.** As expected debulking surgery provided no survival benefit over untreated control. TAGS shows significantly improved long-term survival over white light

and other control groups (****P < 0.0001). For control and debulking group n = 7; for white light group n = 15; for TAGS group n = 18. See Movies in the Supplemental Materials for real-time surgical resection of HN5 tumours.

Author Manuscript

Author Manuscript

Author Manuscript

Author Manuscript

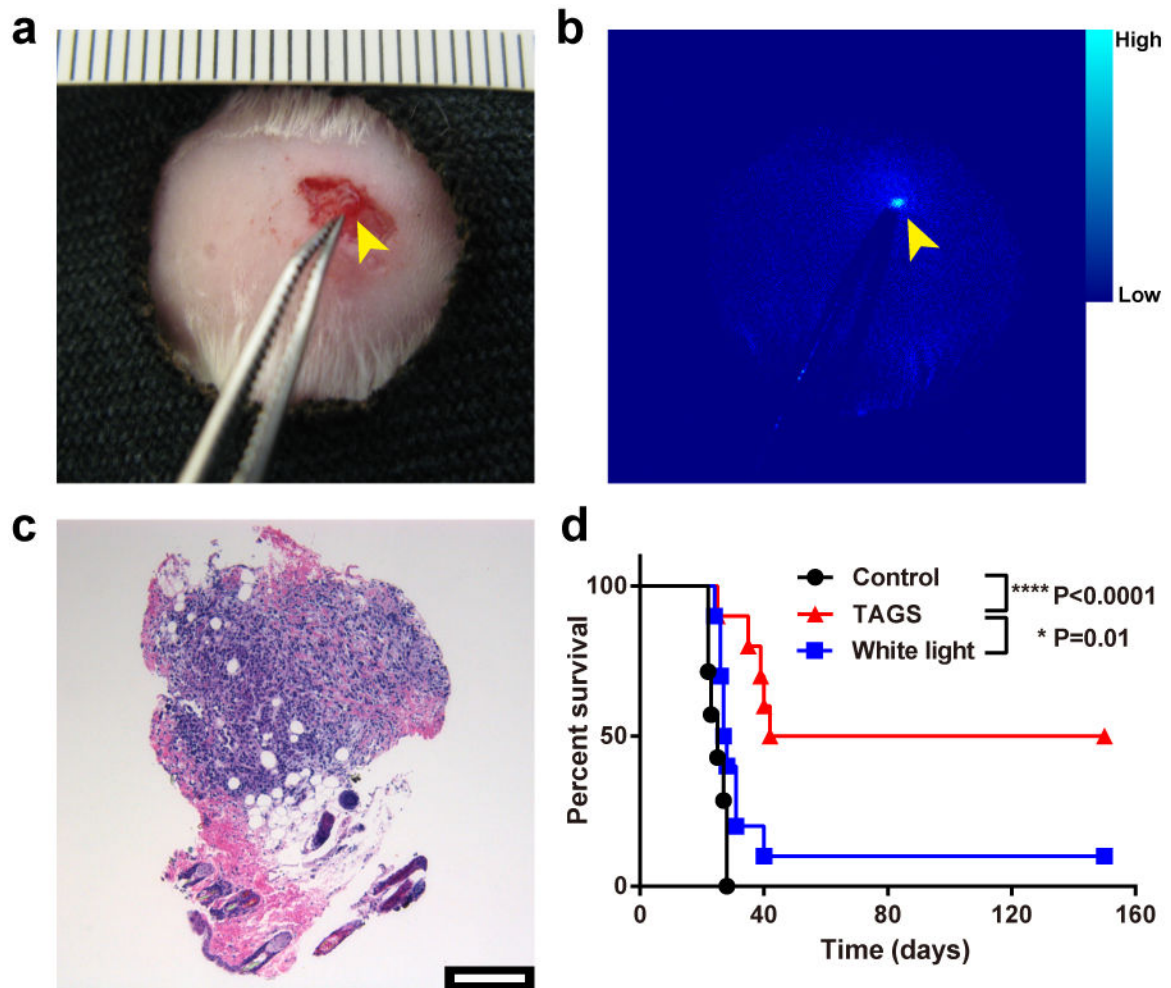


Figure 5. Tumour acidosis guided surgery in mice bearing small occult breast tumour nodules
 Tumour foci (< 1 million cells) was visible under SPY camera (**b**) but not by visual detection (**a**). **c**, A representative histology section of a small breast tumour nodule resected during TAGS; scale bar = 200 μ m. **d**, Kaplan-Meier curve demonstrates significantly improved long-term survival by TAGS over white light and untreated control groups. For control groups $n = 7$; white light and TAGS groups $n = 10$; $*P < 0.05$, $****P < 0.0001$. See Movies in the Supplemental Materials for real-time surgical resection of small occult breast tumours.

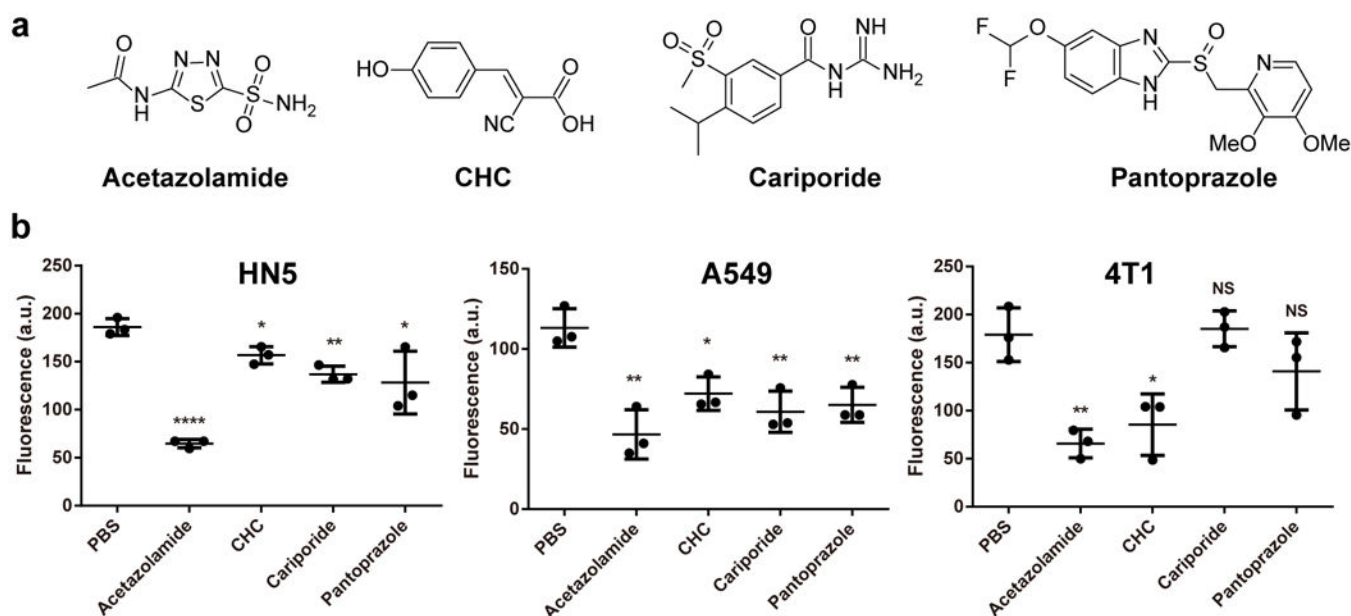


Figure 6. Evaluation of small molecular inhibitors targeting different tumour acidosis pathways by PINS

a. Chemical structures of selected small molecular inhibitors and their corresponding protein targets in parenthesis: acetazolamide (CAIX), α -cyano-4-hydroxycinnamate or CHC (MCT), cariporide (NHE1) and pantoprazole (proton pump). **b.** Quantification of PINS signals in HN5, A549 and 4T1 tumour-bearing mice after injection of PBS or tumour acidosis inhibitors. NIR fluorescence images are shown in Supplementary Fig. 11. Data are presented as individual data points plus mean \pm s.d. ($n = 3$); * $P < 0.05$, ** $P < 0.01$, **** $P < 0.0001$, NS = not significant. CAIX inhibition by acetazolamide resulted in the most efficient suppression of tumour acidosis in all three models.